Treading in the Limited Stability Regime of Lanthanum Strontium Ferrite — Reduction, Phase Change and Exsolution

Thomas Götsch[a,b,c], Norbert Köpfle[c], Lukas Schlicker[d], Emilia A. Carbonio[b,e], Michael Hävecker[a,b], Axel Knop-Gericke[a,b], Robert Schlögl[a,b], Maged F. Bekheet[d], Aleksander Gurlo[d], Andrew Doran[f], Johannes Bernardi[g], Bernhard Klötzer[c], and Simon Penner[c]

[a] Max Planck Institute for Chemical Energy Conversion, Department of Heterogeneous Reactions, Stiftstraße 34–36, 45470 Mülheim an der Ruhr, Germany
[b] Fritz Haber Institute of the Max Planck Society, Department of Inorganic Chemistry, Faradayweg 4–6, 14195 Berlin, Germany
[c] University of Innsbruck, Department of Physical Chemistry, Innrain 52c, 6020 Innsbruck, Austria
[d] Fachgebiet Keramische Werkstoffe / Chair of Advanced Ceramic Materials, Institut für Werkstoffwissenschaften und -technologien, Technische Universität Berlin, 10623 Berlin, Germany
[e] Helmholtz-Zentrum Berlin für Materialien und Energie, Catalysis for Energy, 12489 Berlin, Germany
[f] Advanced Light Source, Lawrence Berkeley National Laboratory Berkeley, CA 94720-8229, USA
[g] University Service Center for Transmission Electron Microscopy, TU Wien, 1040 Vienna, Austria

We present an *in situ* investigation of the iron exsolution from lanthanum strontium ferrite perovskites. Using in situ X-ray diffraction experiments at the synchrotron, the exact onset of exsolution was determined by a change in the lattice parameter before any iron reflexes become visible. For an initially orthorhombic thin film, on the other hand, a phase transition to a fluorite/rock-salt structure is observed to occur during the exsolution. Also, a difference in the iron oxidation states between bulk and surface is found since photoelectron spectroscopy and X-ray absorption spectroscopy both indicate the existence of the Fe(III)/Fe(II) couple in oxidation/reduction cycles, whereas magnetic measurements would suggest Fe(IV)/Fe(III).

Introduction

In recent years, perovskite materials (ABX_3) have gained a lot of attention in the energy sector since their compositional flexibility can lead to a variety of technically relevant properties (1,2). For instance, the oxides (ABO_3) can be ionic conductors or even mixed ionic and electronic conductors (MIECs), as is the case with lanthanum strontium ferrite ($La_xSr_{1-x}FeO_{3-\delta}$, LSF). Being able to conduct both electrons as well as oxygen anions makes these materials perfectly suitable for solid oxide fuel cell (SOFC) anodes, where the active surface area is increased drastically: for a pure electronic conductor, the reaction is limited to the triple phase boundary between the anode, electrolyte and the gas

phase, whereas, in the case of a MIEC, it can occur at the whole surface that is accessible to the fuel.

However, it has been shown that exsolution of the B site metal from the perovskite (i.e. its migration to the surface) can occur under reducing conditions, forming metallic nanoparticles at the surface (3). This effect was also observed for LSF, leading to the formation of iron nanoparticles of different morphologies (4,5). While this exsolution process can be beneficial in that it creates a supported metal/oxide catalyst system *in situ* (6,7), in the case of SOFCs, it can also lead to deactivation of the cell due to structural instabilities and cracking since the fuels employed usually act as reducing agents.

Thus, it is necessary to gain information about exsolution phenomena at a fundamental level in order to be able to gain control over it. This way, it might be possible to exsolve the particles while preventing a complete breakdown of the cell, hence significantly improving the activity of the cell. Here, we present a comprehensive *in situ* study of the crystallographic and electronic properties prior to and during the iron exsolution in lanthanum strontium ferrite ($La_{0.6}Sr_{0.4}FeO_{3-\delta}$).

Experimental

Commercially available lanthanum strontium ferrite ($La_{0.6}Sr_{0.4}FeO_{3-\delta}$, Sigma Aldrich) was used for the experiments on powders.

Thin films were deposited by ion beam sputtering using a self-built direct current ion beam sputter source (8,9). This source was fitted to a modular high vacuum chamber with a base pressure in the 10^{-7} hPa range (10). The above-mentioned powder was pressed to a pellet (diameter: 10 mm) and used as a sputtering target. The sputter source was operated in an argon pressure of 5×10^{-5} hPa and with an ion energy of 2 keV (11). The films were deposited onto freshly cleaved NaCl(001) single crystal substrates that were heated to 573 K resistively by a Ta foil. The films could subsequently be floated off the crystals by dissolving the sodium chloride in water, which further allowed the films to be scooped up from the water surface using TEM grids (gold, 400 mesh) (10).

In situ X-ray diffraction (XRD) experiments were carried out at beamline 12.2.2 at the Advanced Light Source. Diffractograms were acquired at 25 keV ($\lambda = 0.4959$ Å) using a Perkin Elmer XRD 1621 flat panel detector and quartz capillaries (500 μm) were used as sample compartments, while the gas (1 atm) was fed using 300 μm capillaries. The setup is described in more detail in references (12,13).

Transmission electron microscopy (TEM) was performed using a ThermoFisher Scientific Tecnai F20 S-TWIN, equipped with a Schottky source and a double tilt heating holder (Gatan, maximum temperature of 1273 K and heating rate of several hundreds of K min^{-1}). This instrument was used to record temperature-programmed selected area electron diffraction (SAED) patterns.

In situ core level spectroscopy (X-ray photoelectron spectroscopy (XPS) and X-ray absorption spectroscopy (XAS)) experiments were conducted at the ISISS-PGM beamline at BESSY II at gas pressures of 0.3 hPa. Photoelectron spectra were acquired

using a differentially pumped Specs Phoibos 150 NAP hemispherical sector analyzer. The samples (pellets with 10 mm diameter) were heated by irradiation of the backside with an infrared laser, while the temperature was measured using a K-type thermocouple and a pyrometer. For near-edge X-ray absorption fine structure (NEXAFS) measurements, signals were acquired in Auger electron yield (AEY) and total electron yield (TEY) modes. NEXAF spectra of different iron oxidation states were also simulated using XCLAIM (14). The respective parameters are discussed elsewhere (11).

Results and Discussion

Crystallographic Investigation

We conducted synchrotron-based temperature-programmed XRD experiments in reducing atmospheres in order to understand the crystallographic prerequisites for the exsolution to take place.

Selected powder XRDs during heat treatment in a 5% H_2/Ar mixture from room temperature (bottom) up to approximately 950 K (top-most) are shown in Figure 1A. At room temperature, the diffractogram can be assigned to a single phase, the rhombohedral structure (space group no. 167, *R-3c* (15)). Along the temperature axis, most of the reflexes exhibit a nonlinear shift to lower 2θ values – while a linear one would be expected due to thermal expansion, they exhibit sigmoid-like changes in their positions. This is made clearer in Figure 1B, where selected reflexes are extracted: in i), the rhombohedral 2-10 and 104 reflexes are shown (15). These lie so close together that they cannot be resolved in this diffractogram. However, the resulting sum peak appears very broad with a plateau-like top. At higher temperatures (towards the top in the graph), the peak position undergoes a curve-like shift before appearing much sharper in the end. This is due to a phase transition to the cubic perovskite phase (space group no. 221 *Pm-3m* (16)), which only exhibits a single reflex (110) at this 2θ value (5,17). This effect is even more pronounced in panel iii), where the two peaks in the rhombohedral state (4-1-4 and 3-1-8) are separated more at low temperatures. For these reflexes, the distinct curvature of the nonlinear change in position can be observed very clearly.

The same is the case for panel ii), where the rhombohedral 20-4 as well as the cubic 200 reflexes are shown. Here, both phases only exhibit a single reflex, i.e. the reflex shift is not influenced by different expansion coefficients of different lattice planes when multiple reflexes overlap. Furthermore, there is a small reflex emerging at approximately 14.0°, which stems from the exsolved iron particles (Fe 100, space group no. 229, *Im-3m* (18)).

Since, in both the rhombohedral and the cubic phases, there is only a single reflex underneath the peak at about 14.8°, it was used to analyze the peak shift more closely. In Figure 2A, the peak position (in terms of the lattice spacing *d*) is given as a function of the temperature. The curve has three major areas: a linear behavior at low temperatures, corresponding to the linear thermal expansion of the rhombohedral phase, then a curve between approximately 450 and 700 K, followed by another linear shift at high temperatures (thermal expansion of the cubic phase). The curve in between is the result of a number of complex processes, including distortions in the lattice, the partial

coexistence of both phases, and oxygen loss in the reductive environment. For the linear regions, fits are added to the plot to determine the thermal expansion coefficients, which leads to an apparent isotropic coefficient of expansion of 9.21×10^{-6} nm K^{-1} for the rhombohedral phase.
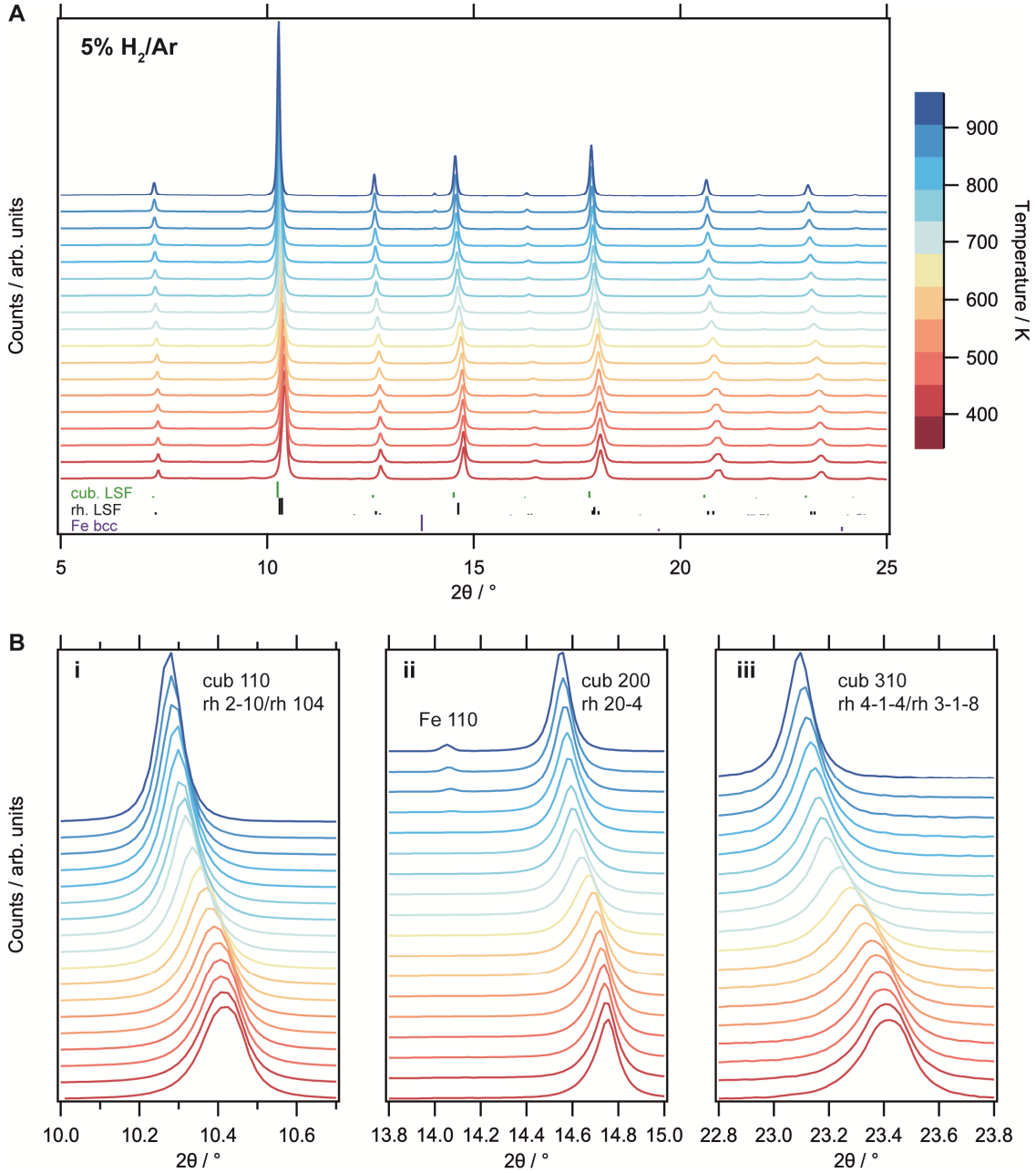

Figure 1. In situ XRD data of the initially rhombohedral LSF powder. A) Exemplary diffractograms at different temperatures in 5% H$_2$/Ar. B) Close-up on some reflexes highlighting the phase transformation and the iron exsolution. Based on data from (5).
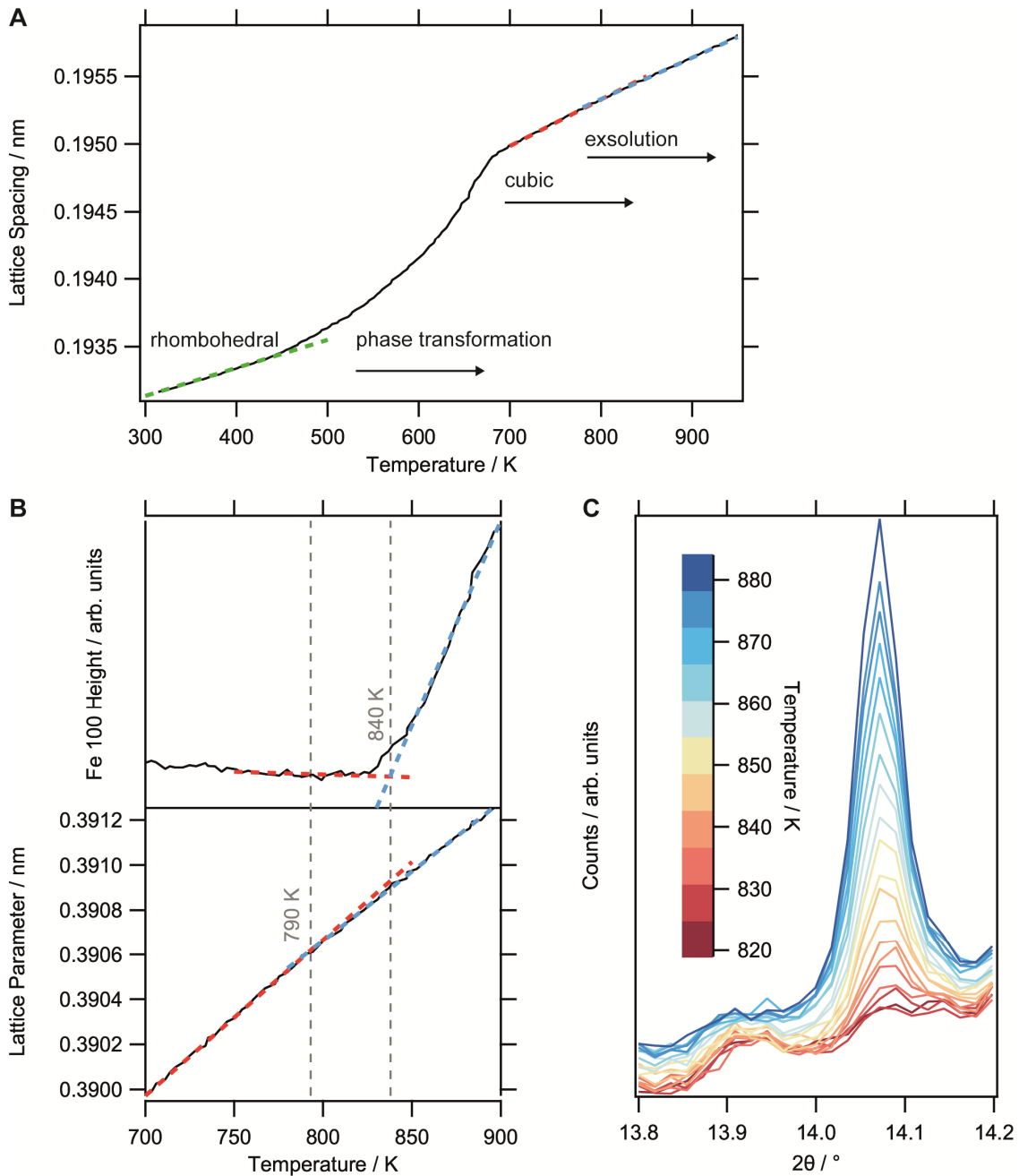
Figure 2. A) Lattice spacing changes for the rhombohedral 20-4 and the cubic 200 reflexes, as obtained by peak fitting of the reflex at approximately $2\theta = 14.8°$. The dashed lines represent fits to the linear ranges, allowing to determine coefficients of expansion. B) The two apparent coefficients of expansion of the cubic phase (lower panel) and the peak height of the Fe 100 reflex (upper panel) yield complementary data about the onset of the exsolution. C) The Fe 100 reflex intensity increases with temperature.

The apparently linear region in the cubic phase can be shown to actually consist of two separate linear areas: the first right after the sharp kink in the curve (fitted by the red dashed line) and a second one above approximately 800 K (blue dashed line). In order to make this clearer, the respective region is magnified in Figure 2B (lower panel).

Additionally, the lattice spacing was converted to the cubic lattice parameter *a*. In the beginning, the lattice expands linearly with a slope of $6.95(9) \times 10^{-6}$ nm K^{-1}, while the thermal expansion is $6.19(4) \times 10^{-6}$ nm K^{-1} at higher temperatures – i.e. there is a significant difference with respect to the error of the fit.

These two separate linear regions can be explained by two different processes: between 700 and 800 K, the thermal expansion of the cubic perovskite appears to take place (including oxygen loss), while above approximately 800 K, iron exsolution starts. The migration of iron ions from the lattice will decrease the unit cell volume, hence the apparently lower thermal expansion. As a test of this hypothesis, the upper panel shows the (background-subtracted) height of the Fe 100 reflex (the respective region of the diffractogram is shown in Figure 2C). Here, the onset of the peak growth is at approximately 840 K while the intersection of the linear fits to the lattice parameter is at 790 K. There is excellent agreement regarding the onset of the iron exsolution, especially if one considers that the appearance of the Fe 100 reflex in the XRD requires a certain crystallite size, whereas the effects on the lattice expansion are noticeable as soon as the first iron ions leave the lattice. Hence, the exsolution actually starts at around 790 K, whereas the particles formed at the surface become big enough to be detected *via* XRD at about 840 K.
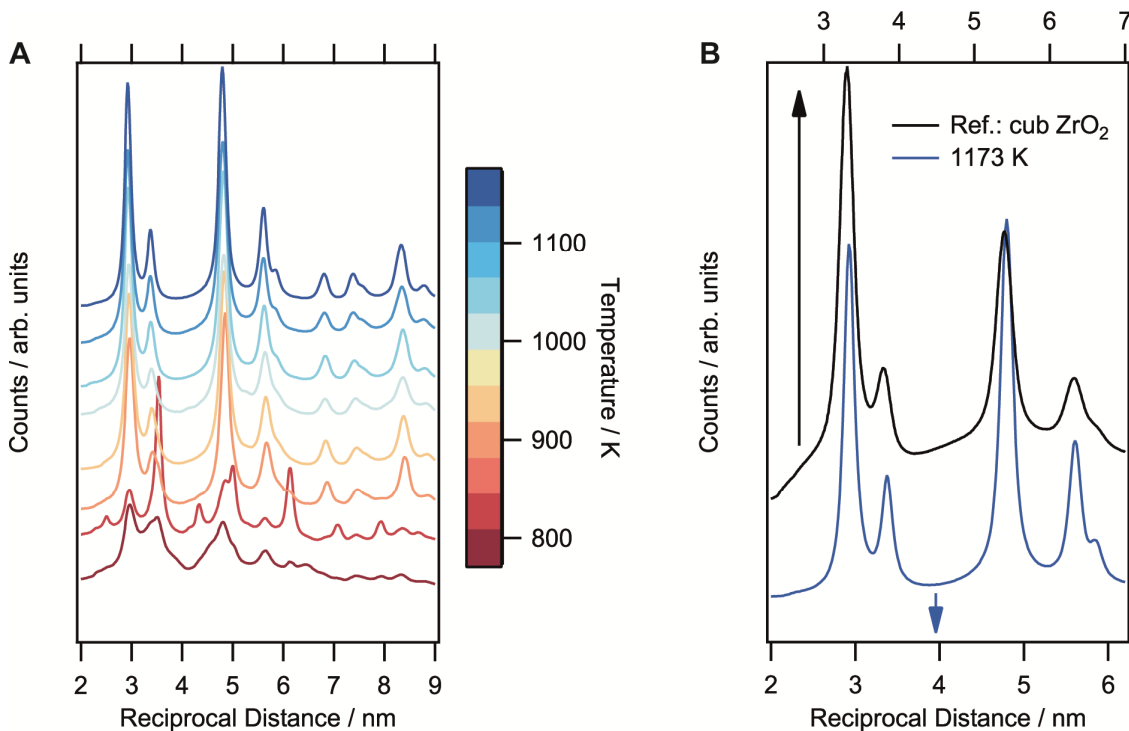

Figure 3. A) Selected SAEDs from a heating experiment of the orthorhombic thin film in high vacuum. Based on ref. (11). B) Comparison of the diffractogram obtained at the highest temperature (lower curve) with that of a fluorite structure (cubic zirconia, from ref. (8)).

As an alternative system to the rhombohedral powder, an orthorhombic thin film (space group no. 51, *Pmma* (19)) was used. This specimen was heated in the reducing conditions of the high vacuum of a TEM. This film was previously shown to be

amorphous when deposited, but could be crystallized upon calcination while retaining a large degree of epitaxy (20). The azimuthally integrated selected area electron diffraction patterns of the *in-vacuo* heating experiment are shown in Figure 3A. At the lowest temperature displayed (773 K), the initially amorphous structure begins to crystallize; hence, the peaks still appear very broad. The crystallization of the orthorhombic lattice is subsequently completed at 823 K, at which point the exsolution starts as well (11). At 873 K, however, the diffraction pattern changes again completely, with shifted intensity ratios and some previously prominent peaks now completely missing. Evidently, a phase transition to a second crystalline phase takes place between 823 and 873 K (and above 1023 K, the exsolution of iron particles starts from this phase (11)). The exact identity of this phase is as-of-yet still unknown, but there is strong evidence that it is either a fluorite or a rock-salt structure, which both crystallize in space group *Fm-3m* (no. 225): in Figure 3B, the diffraction pattern profile recorded at 1173 K is compared to that of a cubic zirconia thin film (space group 225, *Fm-3m* (8)). To facilitate the comparison, the respective *x*-axes were shifted and scaled to get a good overlap of the diffraction patterns. The peak positions as well as their relative intensities show an extreme agreement. The peaks are better resolved for the diffractogram of the decomposed perovskite than for the cubic ZrO_2 as the latter was a nanocrystalline film (resulting in broader rings in the SAED pattern) measured at room temperature, whereas the present sample sintered at these high temperatures.

Electronic structure

In a previous work, the iron oxidation states were determined using *ex situ* XPS (5,17). According to this method, the iron is initially in the +III state and gets subsequently reduced to +II during thermal treatment in hydrogen. Above a certain temperature, however, the exsolution starts, which is visible by an increase Fe(III) fraction again (because the nanoparticles readily oxidize in ambient conditions during the transport to the spectrometer) (5,17). However, this is in disagreement with published Moessbauer spectroscopy data (21,22): these magnetic measurements all suggest Fe(IV) in the oxidized state and Fe(III) in the reduced one. In order to investigate this discrepancy further, *in situ* near-ambient pressure XPS and XAS was employed at pressures of 0.3 hPa.

Temperature-dependent XPS spectra of the Fe $2p_{3/2}$ region are given in Figure 4A. In order to get a reliable reference state and remove surface carbon, the sample was initially heated to 873 K in 0.3 hPa of oxygen. Afterwards, it was cooled down to room temperature and ramped up in the same partial pressure of hydrogen. The spectrum acquired in H_2 at 773 K shows virtually no changes to that of the pre-oxidized state, suggesting that the temperature is too low to significantly reduce the specimen. However, there is a noticeable shift to lower binding energies at 873 K and the spectrum can be fitted almost solely by Fe(II) (11). At 973 K, only Fe(II) is present with a small shoulder of metallic iron appearing at about 706 eV.

At this temperature, time-resolved measurements were conducted, which are displayed in Figure 4B: the lower-binding-energy side shoulder becomes more prominent as the exsolution proceeds over time, which was previously shown to follow an Avrami-type behavior and to be in excellent agreement with the Fe 110 intensity evolution obtained from XRD (11).
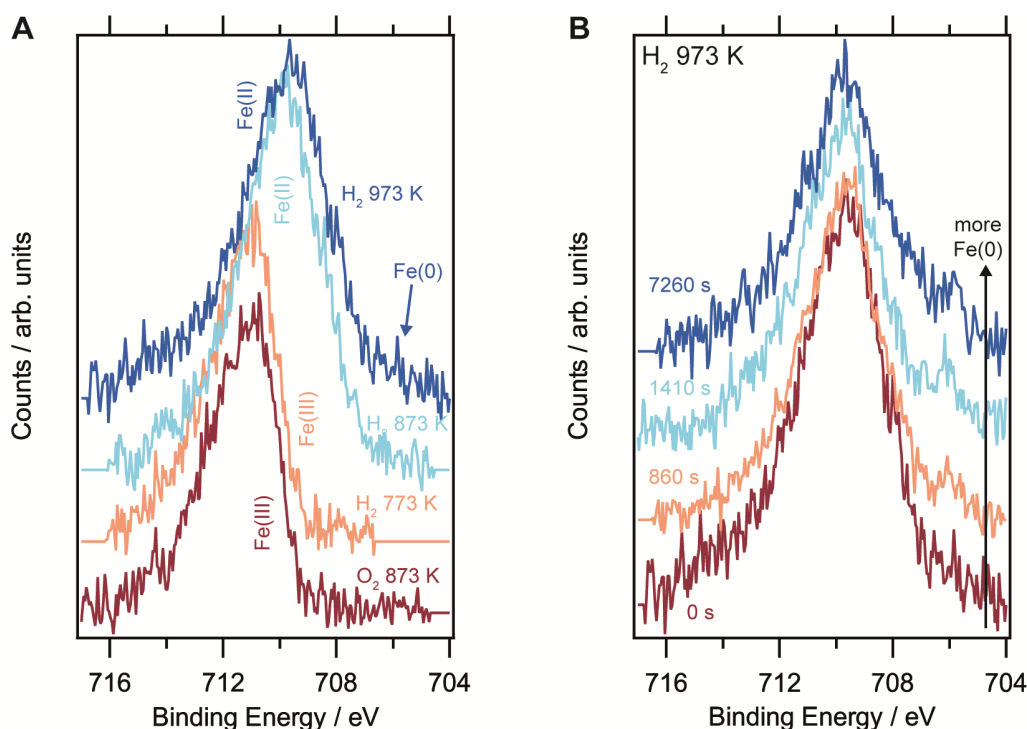
Figure 4. *In situ* XPS data (background-subtracted). A) Temperature-programmed spectra of the Fe $2p_{3/2}$ region for an oxidation-reduction cycle. B) Time-resolved spectra acquired during reduction in hydrogen at 973 K.

Since the respective L edges in X-ray absorption of early transition metals are often more sensitive to chemical changes than the 2p regions in XPS, we also conducted XAS in near-ambient pressure conditions to further support the results obtained by XPS. As seen in Figure 5A, the Fe $L_{2,3}$ edge undergoes significant changes upon reduction: in the pre-oxidized state, it resembles the calculated absorption edge for Fe(III) (see panel B where theoretical spectra calculated *via* the multiplet ligand-field theory are shown (11)). If it was Fe(IV), there would have to be a strong shoulder after the white line and the splitting as well as the intensity ratio of the peaks in the L_2 edge would have to be significantly different, as seen from the calculations. Upon reduction at 773 K, a slight increase in intensity in the pre-edge feature appears and the post-white-line tail decreases compared to the oxidized state. Both features can be explained by the presence of Fe(II) – see also Figure 5B where the edge for Fe(II) is shifted slightly to lower energies. This becomes more apparent at higher reduction temperatures, which cause the shoulder on the lower energy side of the edge to become more pronounced. Additionally, a strongly increased pre-edge intensity hints at metallic iron. At the highest temperature, 973 K, the general intensity of the edge is also lower. This is most likely due to Ostwald ripening in that the larger sintered particles make more of the iron-depleted perovskite surface accessible to the relatively surface-sensitive TEY signal.
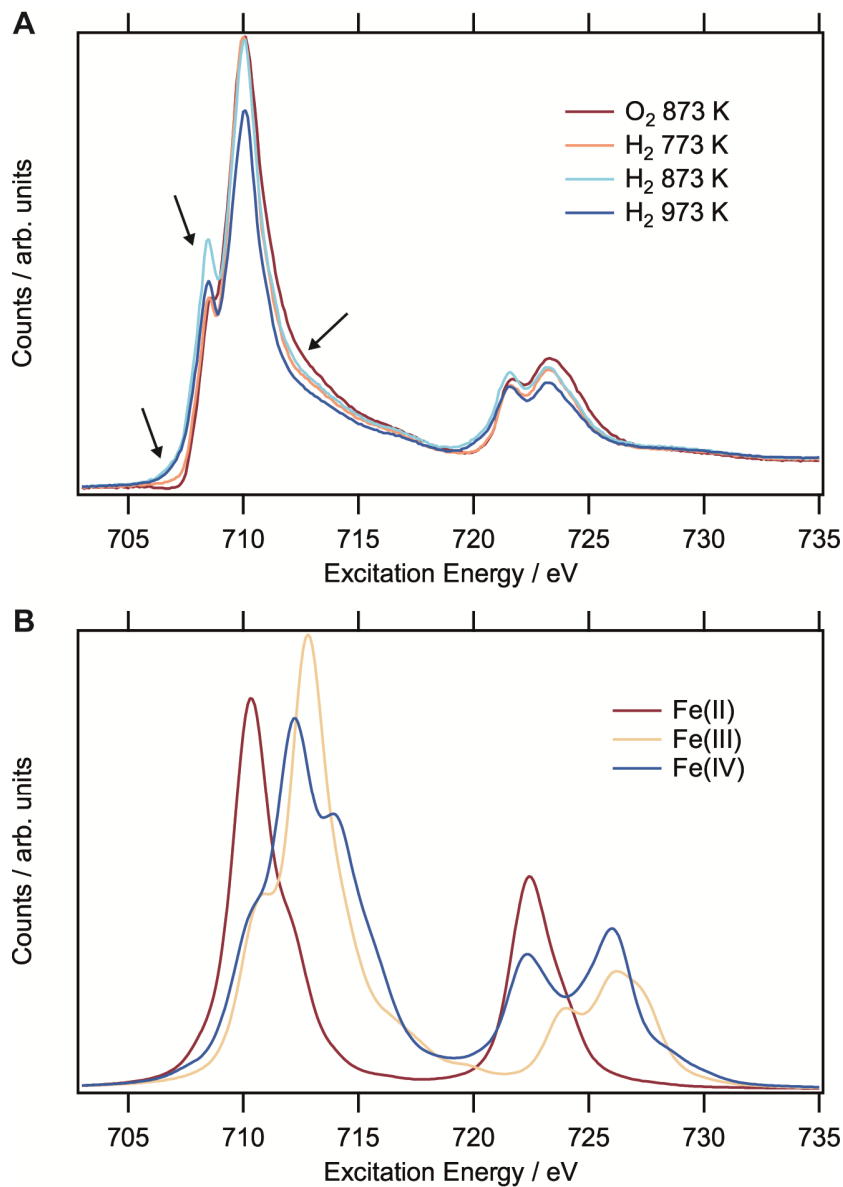
Figure 5. A) Near-ambient pressure X-ray absorption spectra (Fe-L edge) acquired in 0.3 hPa of gas (oxygen or hydrogen) in total electron yield. B) Calculated spectra for different iron oxidation states.

Thus, NEXAFS confirms what was observed with XPS in that no Fe(IV) can be detected, which is in direct disagreement with magnetic measurements. However, it is feasible that the surface states are different because all magnetic measurements like Moessbauer spectroscopy or Neutron diffraction (11) are bulk-sensitive, whereas XPS and NEXAFS in TEY as presented here only probe the outermost regions of the sample. To test this, (partial) fluorescence yield NEXAFS would be required to analyze the bulk as well.

Conclusion

Using *in situ* XRD, a change in the thermal expansion characteristics of lanthanum strontium ferrite was used to pin-point the onset of iron exsolution, which occurs at a temperature about 50 K lower than the appearance of the Fe bcc reflexes (which requires a certain size of the accumulated iron particles to be exceeded). Moreover, a phase transition to the cubic phase is apparently required for the exsolution to occur in the rhombohedral system, whereas, for the thin film, it already took place in the orthorhombic phase before any phase transformation. Thus, in applications where structural stabilities are crucial, it might be possible to prevent the exsolution process from happening if the composition (e.g. the La/Sr ratio) is changed so that the transition to the cubic structure is suppressed.

Contrasting bulk-sensitive *ex situ* Moessbauer spectroscopy and neutron scattering experiments, *in situ* near-ambient pressure XPS and NEXAFS confirmed the absence of Fe(IV) states in the surface-near region, suggesting a difference in the electronic structure between bulk and surface. Here, further studies are needed, for instance with fluorescence yield NEXAFS to also probe the bulk regions of the material since these drastically different electronic structures in the bulk and at the surface are expected to have a big impact on the performance in SOFCs as the bulk will be primarily important for the ionic conduction, but the surface for the electrocatalytic activity itself.

Acknowledgments

References

1. A. P. Ramirez, *Journal of Physics: Condensed Matter*, **9**, 8171 (1997).
2. M. A. Peña and J. L. G. Fierro, *Chemical Reviews*, **101**, 1981 (2001).
3. D. Neagu, G. Tsekouras, D. N. Miller, H. Ménard, and J. T. S. Irvine, *Nature Chemistry*, **5**, 916 (2013).

4. R. Thalinger, M. Gocyla, M. Heggen, B. Klötzer, and S. Penner, *J. Phys. Chem. C*, **119**, 22050 (2015).
5. T. Götsch et al., *RSC Adv.*, **8**, 3120 (2018).
6. R. Thalinger et al., *J. Catal.*, **337**, 26 (2016).
7. R. Thalinger et al., *ChemCatChem*, **8**, 2057 (2016).
8. T. Götsch, W. Wallisch, M. Stöger-Pollach, B. Klötzer, and S. Penner, *AIP Adv.*, **6**, 025119 (2016).
9. T. Götsch, B. Neumann, B. Klötzer, and S. Penner, *Surface Science*, **680**, 52 (2019).
10. T. Götsch et al., *Review of Scientific Instruments*, **90**, 023902 (2019).
11. T. Götsch et al., *Phys. Chem. Chem. Phys.*, **21**, 3781 (2019).
12. L. Schlicker et al., *Rev. Sci. Instrum.*, **89**, 033904 (2018).
13. A. Doran et al., *Rev. Sci. Instrum.*, **88**, 013903 (2017).
14. J. Fernández-Rodríguez, B. Toby, and M. van Veenendaal, *J. Electron Spectrosc. Relat. Phenom.*, **202**, 81 (2015).
15. S. E. Dann, D. B. Currie, M. T. Weller, M. F. Thomas, and A. D. Al-Rawwas, *J. Solid State Chem.*, **109**, 134 (1994).
16. W. C. Koehler and E. O. Wollan, *J. Phys. Chem. Solids*, **2**, 100 (1957).
17. T. Götsch et al., *ECS Trans.*, **78**, 1327 (2017).
18. Z. S. Basinski, W. Hume-Rothery, and A. L. Sutton, *Proc. R. Soc. London, Ser. A*, **229**, 459 (1955).
19. P. D. Battle, T. C. Gibb, and P. Lightfoot, *J. Solid State Chem.*, **84**, 237 (1990).
20. T. Götsch et al., *Appl. Surf. Sci.*, **452**, 190 (2018).
21. Z. Chu et al., *J. Appl. Phys.*, **91**, 7938 (2002).
22. Sk. Sabyasachi et al., *Phys. Rev. B*, **86**, 2761 (2012).